ACS APPLIED MATERIALS & INTERFACES

www.acsami.org

Research Article

Exosomes Derived from Bone Marrow Mesenchymal Stem Cells Encapsulated in M2 Macrophage Cell Membrane Targeted to Inhibit Joint Periprosthetic Inflammation

Zheyu Zhang,[†] Tianliang Ma,[†] Qimeng Liu, Jiangyu Nan, Guanzhi Liu, Yute Yang, Yihe Hu,* and Jie Xie*

Cite This: *ACS Appl. Mater. Interfaces* 2025, 17, 22279−22292

Read Online

ACCESS | Metrics & More | Article Recommendations | Supporting Information

ABSTRACT: Periprosthetic osteolysis (PPOL) is a serious complication following total joint replacement surgery, and exploring treatments for this complication is of significant societal importance. Exosomes derived from bone marrow mesenchymal stem cells (BMSC-Exos, Exos) have diverse cellular functions, such as inhibiting osteoclast formation, suppressing inflammation progression, and promoting M2 macrophage polarization. However, standalone Exosomes are easily recognized and phagocytosed by the immune system, have a short half-life, and lack specificity. This study is based on the homing effect possessed by M2 macrophages under the regulation of various factors. By combining this with cell membrane encapsulation technology and embedding BMSC-Exos within the membrane of M2 macrophages (M2M-Exos), the aim is to inhibit inflammation and treat PPOL. It was found that M2M-Exos can target the PPOL area, enhancing the therapeutic effects of the BMSC-Exos and reducing wear particle-induced cranial osteolysis. Additionally, M2M-Exos provide immune camouflage through the cell membrane, allowing the BMSC-Exos to evade clearance by the mononuclear macrophage system in the body. Therefore, the study demonstrates the targeting ability of M2M-Exos and their unique role in preventing PPOL. These biomimetic nanoparticles establish a targeted nanodrug delivery system for PPOL treatment.

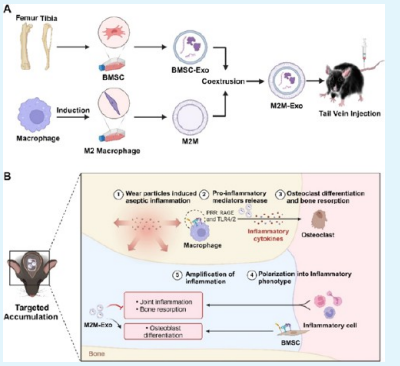

KEYWORDS: *exosomes derived from bone marrow mesenchymal stem cells, M2 macrophages, targeted therapy, anti-inflammation, periprosthetic osteolysis*

1. INTRODUCTION

The increasing aging population and traumatic accidents have led to a global rise in total joint replacement surgeries, yet periprosthetic osteolysis (PPOL),[1] a common complication causing aseptic loosening and prosthesis failure, remains a major concern. Studies have indicated that the incidence of aseptic loosening following total joint replacement surgery can be as high as 20.3%. it accounts for 12.8% of total knee arthroplasty complications in the U.S., second only to infection.[2] In a single-center clinical follow-up study,[3] 79 out of 250 patients (31.6%) undergoing primary total ankle replacement surgery experienced PPOL.[4] The average cost of revision surgery for joint prostheses is approximately $35,000.[5] After joint replacement surgery, prostheses restore joint function and reduce joint pain, but wear particles from materials (metals, ceramics, etc.) or surrounding tissues form at the bone-prosthesis interface. Even ceramics generate nanoscale fragments during movement, confirming widespread particle generation risks.[6] These particles disrupt microenvironment balance, triggering chronic inflammation and PPOL.[7−9] Once wear particles infiltrate surrounding tissues, they can be recognized and engulfed by immune cells such as macrophages. Activated macrophages that engulf wear particles release inflammatory cytokines, chemokines, reactive oxygen species (ROS), tumor necrosis factor-α (TNF-α), interleukin-1beta (IL-1β), interleukin-6 (IL-6), interleukin-17 (IL-17), and interferon-γ (IFN-γ), all of which are critical factors inducing PPOL.[10,11] It has been reported that poly(methyl methacrylate) wear particles around prostheses can enhance the expression of M1 macrophages, reduce the expression of M2 anti-inflammatory macrophages, and increase local inflammation.[12] Similarly, in bone cement prostheses, macrophages attempting to engulf bone cement particles stimulate high levels of TNF-α release, thereby enhancing a pro-inflammatory environment.[13,14] The release of inflammatory mediators and cytokines can activate and enhance the function of bone-resorbing cells (such as macrophages and osteoclasts),

Received: December 29, 2024
Revised: March 22, 2025
Accepted: March 24, 2025
Published: April 1, 2025

https://doi.org/10.1021/acsami.4c22304
ACS Appl. Mater. Interfaces 2025, 17, 22279−22292

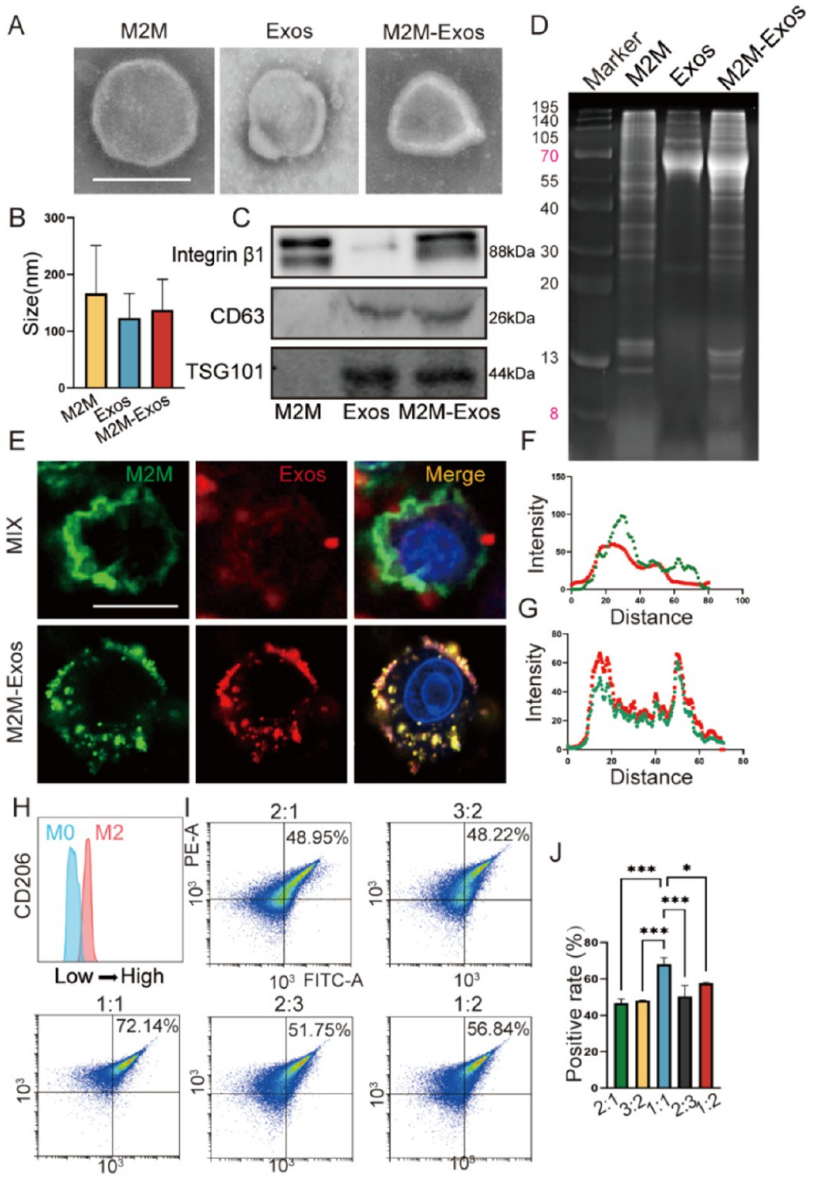

Figure 1. Construction and characterization of M2M-Exos. (A) TEM images of M2M, BMSC-Exos, and M2M-Exos. (Scale bar, 150 nm). (B) NTA measurements of particle diameters for BMSC-Exos, M2M, and M2M-Exos. (C) Western blot analysis to determine typical surface markers expressed on M2M, BMSC-Exos, and M2M-Exos. (D) Coomassie brilliant blue staining for protein profiling. (E) Typical confocal images of RAW264.7 incubated with M2M-Exos (green for DiO-labeled M2M, red for DiI-labeled BMSC-Exos). (Scale bar,10 μm). (F, G) Co-localization analysis of DiO and DiI in confocal images of A mixture of M2M and BMSC-Exos (F), and M2M-Exos (H). Flow cytometry analysis of CD206 expression. (I) Nanoflow cytometry evaluation of exosome encapsulation efficiency at different material mixing ratios. (J) Quantitative analysis of encapsulation efficiency at different material ratios. (*p < 0.05, **p < 0.01, ***p < 0.001).

leading to increased bone resorption in surrounding bone tissues. In conclusion, there are still many unresolved questions regarding the disease mechanisms of inflammatory microenvironments in PPOL.

Membrane-encapsulated nanoparticle drug delivery systems represent an advanced technology aimed at enhancing drug solubility, stability, bioavailability, and therapeutic targeting.[15] The core principle involves encapsulating drug carriers within nanosized polymers, lipids, or other biocompatible materials to form nanoparticles, which subsequently transport the drug to target tissues or cells. The preparation of cell membrane-encapsulated nanoparticles comprises several steps, including cell membrane extraction, core nanoparticle preparation, and membrane-nanoparticle fusion.[16] Common fusion methods include coextrusion, ultrasound, microfluidic electroporation, and electrostatic attraction.[17] In this study, coextrusion—a prevalent technique for preparing cell membrane-camouflaged nanoparticles—was employed using a porous polycarbonate membrane liposome extruder.[18]

Exosomes (30−200 nm extracellular vesicles) carry mRNAs, miRNAs, and proteins, serving as key mediators of intercellular communication. Cell membrane-encapsulated exosomes have been widely explored for disease theranostics. For instance: Zhang et al.[19] designed tumor membrane-coated polyurethane nanoparticles delivering PLK1 siRNA to suppress cancer; Gao et al.[20] engineered red blood cell (RBC) membrane-camouflaged nanogels targeting miR155 with prolonged circulation; Mu et al.[21] developed stem cell membrane-wrapped polydopamine nanoparticles codelivering DOX and PDL1 siRNA for metastatic prostate cancer, achieving

https://doi.org/10.1021/acsami.4c22304
ACS Appl. Mater. Interfaces 2025, 17, 22279−22292

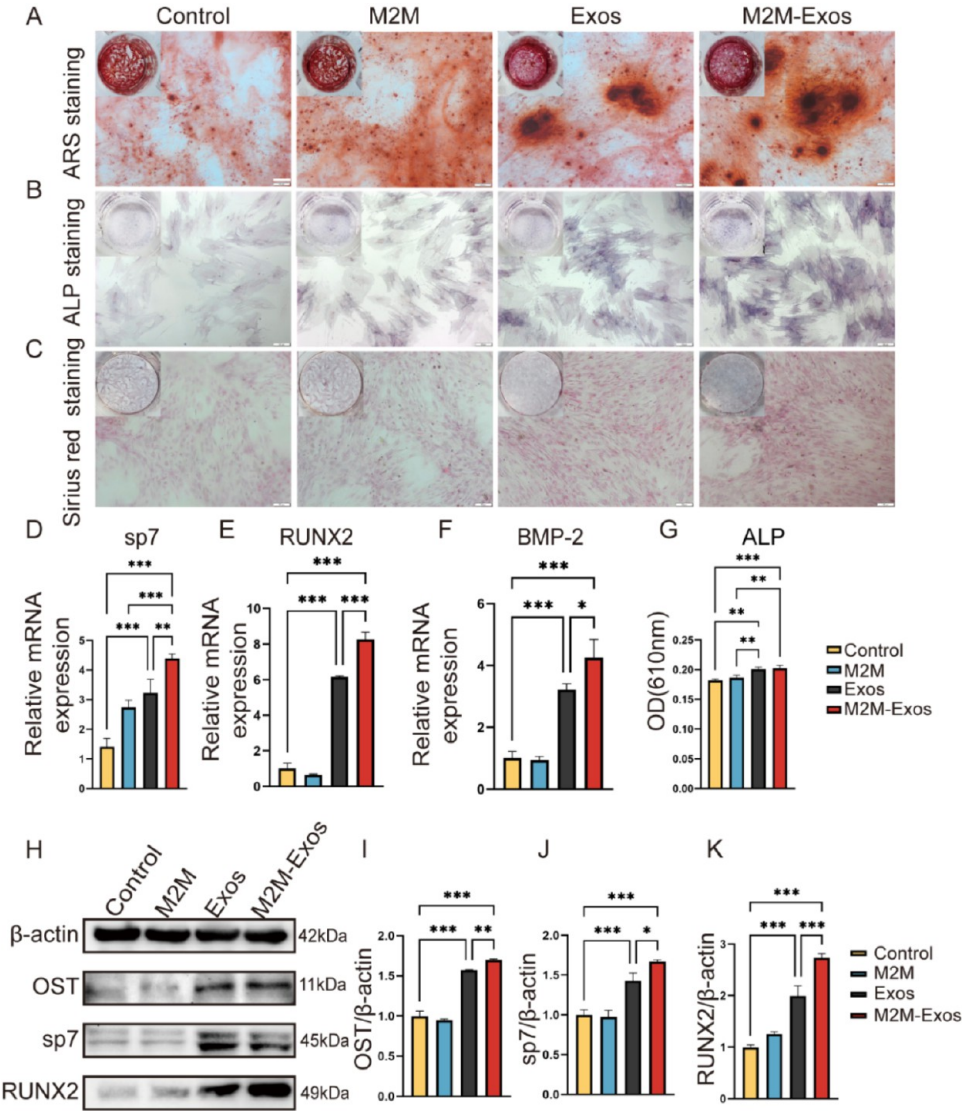

Figure 2. M2M-Exos promote osteogenic differentiation of BMSCs. (M2M: 100 μg/mL, BMSC-Exos: 100 μg/mL, M2M-Exos: 100 μg/mL) (A) ARS staining of BMSCs after 7 days of osteogenic induction. (Scale bar, 100 μm) (B) ALP activity assay of BMSCs after 3 days of osteogenic induction. (Scale bar, 100 μm) (C) Sirius Red staining of BMSCs after 7 days of osteogenic induction. (Scale bar, 100 μm) (D−F) qPCR analysis of osteogenic-related genes (sp7, RUNX2, BMP-2). (G) Quantitative analysis of ALP levels in bone marrow mesenchymal stem cell culture under different treatments. (H) Western blot analysis of osteogenic-related protein expression. (I−K) Quantitative analysis of osteogenic-related protein levels in bone marrow mesenchymal stem cell culture under different treatments. Data are presented as mean ± SD (n = 3/group) (*p < 0.05, **p < 0.01, ***p < 0.001).

synergistic chemoimmunotherapy; Jiang et al.[22] utilized platelet membrane-coated systems to target atherosclerotic plaques, reducing lipid deposition and necrosis. Mesenchymal stem cells are a type of multipotent stem cell with significant roles in adipogenesis, osteogenesis, and chondrogenesis. The biological and therapeutic effects of BMSCs are primarily mediated through paracrine molecules,[23,24] including growth factors, chemokines, cytokines, and exosomes. BMSCs are considered the most effective producers of extracellular vesicles.[25]

BMSC-Exos mediate cell signaling, anti-inflammation, and tissue regeneration,[26] which offer several advantages over BMSCs: no tumorigenicity, microenvironment stability, and reduced side effects.[27−29] Numerous studies have extensively explored the biological functions of BMSC-Exos, demonstrating their positive therapeutic effects in conditions such as heart disease, kidney injury, and ulcers.[30−34] BMSC-Exos can inhibit macrophage-induced inflammation, suppress osteoclast generation, and promote osteogenesis by delivering miR-182−5p inhibitors.[35] However, they are easily recognized and cleared by the immune system upon entry into the body, resulting in a short half-life and limited targeting capabilities. Macrophages, a type of mononuclear cell, play a vital role in inflammation and tissue repair processes.[36] During infection or tissue damage, cytokines such as IL-1β, TNF-α, and IL-8 recruit macrophages to the site of inflammation to perform their respective functions. Macrophages are typically classified into two types: M1 macrophages and M2 macrophages.[37] Macrophages are classified as M1 (pro-inflammatory/phagocytic) or M2 (anti-inflammatory/immune-regulatory), the M2 macrophages cell membrane (M2M) may contain proteins or cellular adhesion molecules with anti-inflammatory properties and targeting abilities in inflammatory regions. Therefore, this study aims to construct M2M-coated BMSC-Exos (M2M-

https://doi.org/10.1021/acsami.4c22304
ACS Appl. Mater. Interfaces 2025, 17, 22279−22292

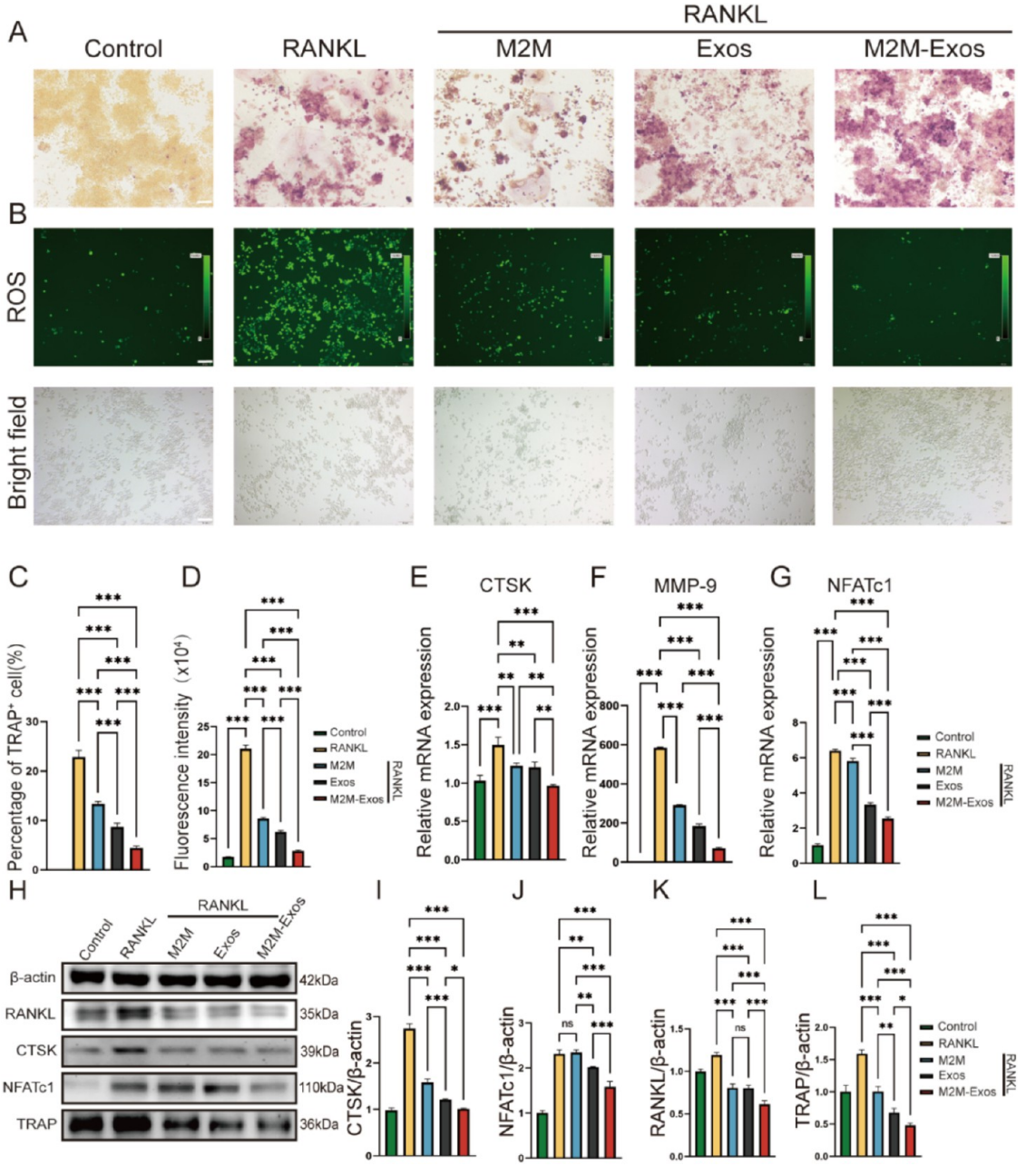

Figure 3. M2M-Exos exhibit inhibitory effects on osteoclast differentiation in RAW264.7 cells. (M2M: 300 μg/mL, BMSC-Exos: 300 μg/mL, M2M-Exos: 300 μg/mL) (A) TRAP staining to assess osteoclast differentiation in RAW264.7 cells. (Scale bar, 50 μm) (B, D) Determination and quantification of intracellular reactive oxygen species. (Scale bar, 50 μm) (C) Percentage of TRAP-positive cells and quantification of TRAP-positive multinucleated (>3 nuclei) osteoclasts. N = 3 samples per group. (E−G) qPCR analysis of osteoclast-related genes (CTSK, NFATc1, MMP-9). (H) Western blot analysis of osteoclast-related protein expression. (I−L) Quantitative analysis of osteoclast-related proteins (RANKL, CTSK, NFATc1, TRAP) in bone marrow mesenchymal stem cell culture under different treatments. Data are presented as mean ± SD (n = 3/group) (*p < 0.05, **p < 0.01, ***p < 0.001).

Exos) using a coextrusion method. By leveraging the targeting ability of M2 macrophage membranes in inflammatory regions, these nanoparticles can exert anti-inflammatory effects and sustain the release of BMSC-Exos at the target site. This approach aims to better inhibit the development of inflammation in osteolysis areas, suppress osteoclast formation, and promote osteogenesis.

2. RESULTS

2.1. Construction and Characterization of M2M-Exos.

A schematic diagram illustrating the construction of M2M-Exos is presented in Graphical abstract A. BMSCs were previously extracted to isolate exosomes from their culture medium, as detailed earlier in this study. Following the induction of RAW264.7 cell differentiation into M2 macrophages, the expression of CD206, a macrophage mannose receptor, was evaluated using flow cytometry (Figure 1H). M2M were then extracted using methods outlined in the literature. Transmission electron microscopy (TEM) showed that M2M-Exos possess a distinct bilayer membrane structure (Figure 1A). Nanoparticle tracking analysis (NTA) displayed the diameters of the particles: approximately 124 nm for

https://doi.org/10.1021/acsami.4c22304
ACS Appl. Mater. Interfaces 2025, 17, 22279−22292

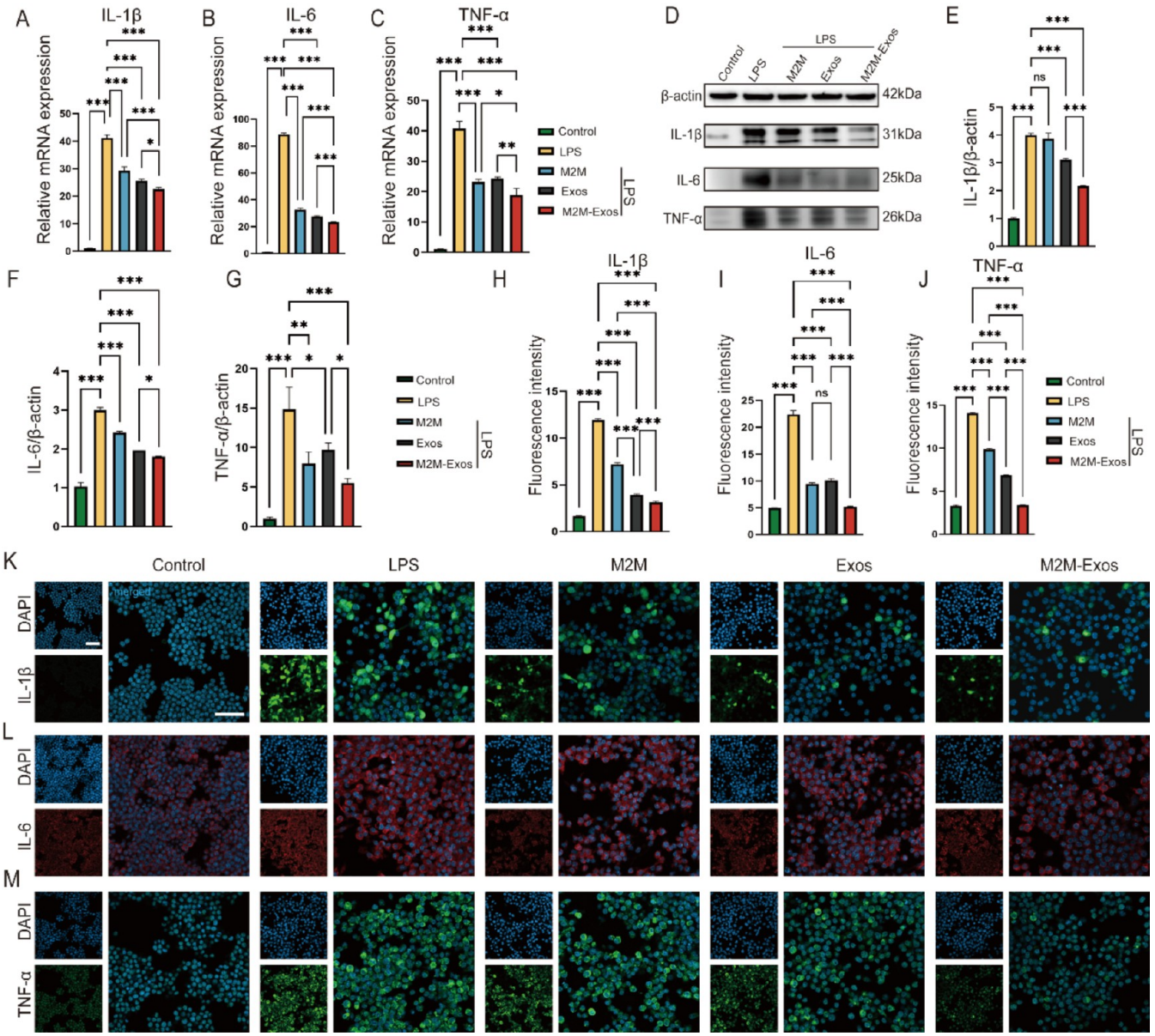

Figure 4. M2M-Exos inhibited inflammation in vitro (A−C) qPCR determination of inflammation-related genes (IL-1β, IL-6, TNF-α). (D) Western blot analysis of the protein expression levels of inflammatory markers (IL-1β, IL-6, TNF-α). (E−G) Quantitative analysis of inflammation-related protein expression in 264.7 cells induced by different cell culture media using Western blot. (H−J) statistical results of Immunofluorescence staining (K−M) Immunofluorescence staining of IL-1β, IL-6, TNF-α in RAW264.7 of different groups. (Scale bar, 50 μm) (*$p < 0.05$, **$p < 0.01$, ***$p < 0.001$).

BMSC-Exos, 167 nm for M2M, and 138 nm for M2M-Exos (Figure 1B). Western Blot analysis was employed to investigate the preservation of M2 macrophage membrane proteins during the coextrusion process, a critical aspect for the biological functionality of M2M-Exos. Coomassie brilliant blue staining demonstrated that the protein profile of M2M-Exos was similar to that of both M2M and BMSC-Exos (Figure 1D), indicating inheritance of their protein expressions. Notably, M2M-Exos contained macrophage-specific protein integrin β1 and exosome-specific proteins TSG101 and CD63 (Figure 1C). To optimize the mixing ratio of M2M and exosomes, various protein ratios were analyzed using nanoflow cytometry. Results indicated that a 1:1 ratio of M2M to exosomes yielded an encapsulation efficiency of approximately 72.14% (Figure 1I,J). Successful preparation and uptake of M2M-Exos by RAW264.7 and BMSC cells were confirmed through labeling M2M with DiO and exosomes with DiI. Laser confocal microscopy revealed colocalization of M2M (green signal) and BMSC-Exos(red signal), resulting in a yellow signal indicating effective merging (Figure 1E). Co-localization analysis of the fluorescence signals demonstrated that the M2M-Exos group exhibited stronger fluorescence colocalization compared to the simple mixing group (Figure 1F,G).

2.2. M2M-Exos Promote Osteogenesis In Vitro. Our study initially explored the potential role of M2M-Exos in osteogenic differentiation of BMSCs. We first observed the phagocytic uptake of M2M-Exos by BMSCs using laser confocal microscopy (Figure S1G,H). The BMSCs were cultured in an osteogenic induction medium containing M2M, BMSC-Exos, and M2M-Exos. The impact of M2M-

https://doi.org/10.1021/acsami.4c22304
ACS Appl. Mater. Interfaces 2025, 17, 22279−22292

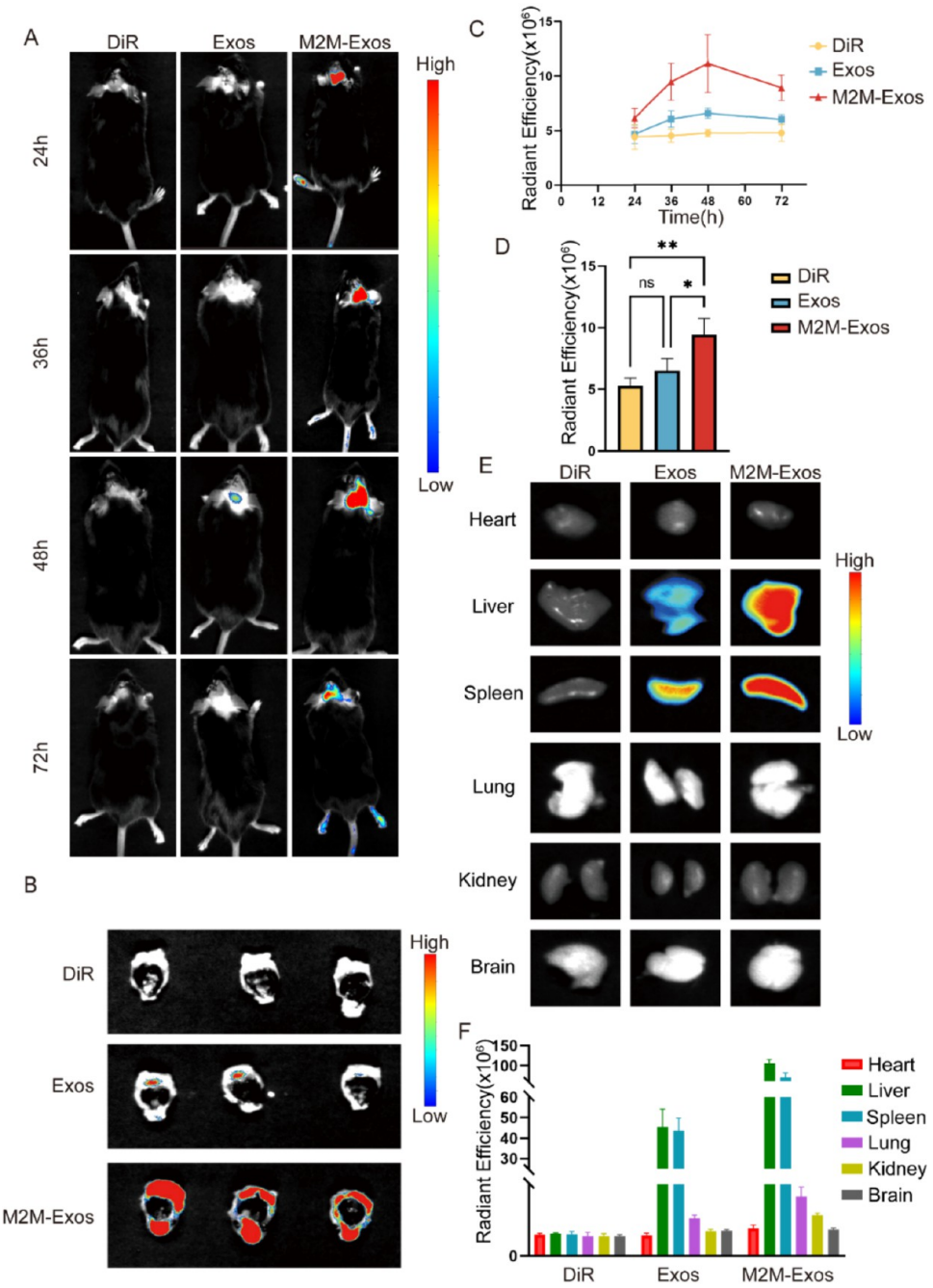

Figure 5. Targeting of M2M-Exos to Ti particle-induced cranial osteolysis sites after intravenous injection (A, C) representative fluorescent images after intravenous injection of DiR-labeled BMSC-Exos (200 μg, 100 μL) and M2M-Exos (200 μg M2M and 200 μg BMSC-Exos, 100 μL), and quantitative analysis of fluorescence intensity (B, D). Representative IVIS images showing the distribution and fluorescence intensity of BMSC-Exos and M2M-Exos in the mouse skull region. (E, F) Typical IVIS images displaying the distribution of BMSC-Exos and M2M-Exos in major organs and the skull after Ti particle-induced cranial osteolysis. (*$p < 0.05$, **$p < 0.01$, ***$p < 0.001$).

Exos on osteogenic induction was assessed using several staining methods including Alizarin Red S (ARS), alkaline phosphatase (ALP), and Sirius Red (Figure 2A−C). Notably, BMSCs exposed to complete osteogenic medium demonstrated a substantial increase in the mRNA expression of bone morphogenetic protein 2 (BMP-2), sp7 (osterix), and RUNX2, particularly under stimulation by BMSC-Exos and M2M-Exos, with M2M-Exos exhibiting a more pronounced induction effect (Figure 2D−F). Additionally, the concentration of ALP in the supernatant was quantified, revealing significant differences among the groups (Figure 2G). Western blot analyses further confirmed that both Exos and M2M-Exos notably enhanced the expression of osteocalcin (OST), sp7, and RUNX2 in BMSC cells, with data presented in Figure 2H−K. These results indicate that while M2M alone did not significantly affect osteogenesis in BMSCs, M2M-Exos had a more substantial impact on ALP activity, calcium nodule formation, and collagen synthesis compared to Exos alone. To evaluate the cytotoxicity of M2M-Exos, cell viability was tested using live/dead cell dual staining and Cell Counting Kit-8 (CCK-8) assays (Figure S1C,F). The assays confirmed that M2M-Exos, at various concentrations ranging from 0, to 400

https://doi.org/10.1021/acsami.4c22304
ACS Appl. Mater. Interfaces 2025, 17, 22279−22292

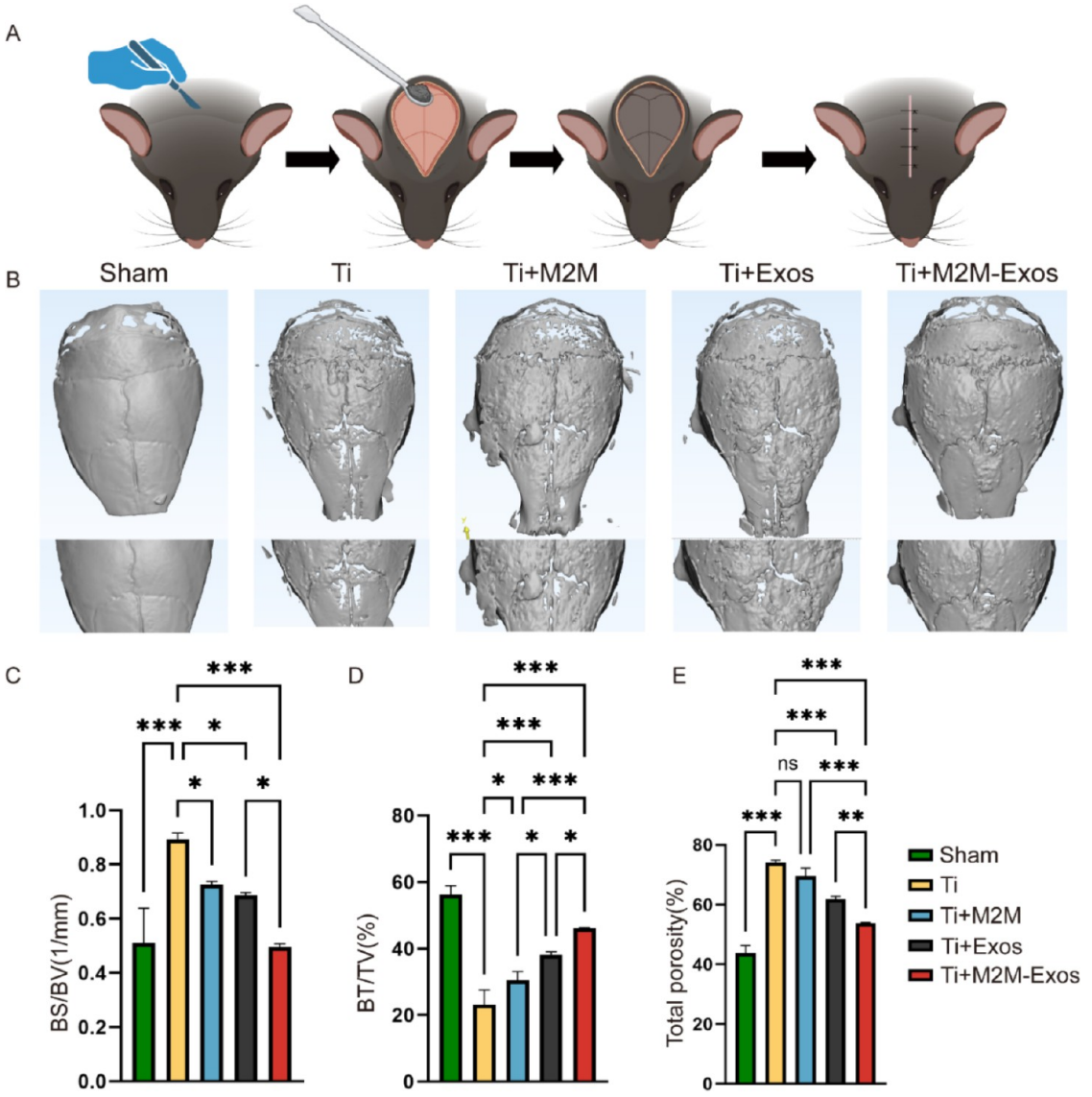

Figure 6. M2M-Exos alleviate Ti particle-induced cranial osteolysis. M2M (200 μg), BMSC-Exos (200 μg), M2M-Exos (200 μg M2M and 200 μg BMSC-Exos) (A) cranial osteolysis induced by Ti particles as described above. DiR, M2M, BMSC-Exos, and M2M-Exos were intravenously injected on day 1, day 8, day 15, and day 22, respectively. (B) Micro-CT three-dimensional reconstruction. (C−E) Measurement of the bone resorption area, quantitative analysis of BS/BV, BV/TV, total porosity (n = 5) (*p < 0.05, **p < 0.01, ***p < 0.001).

μg/mL, were nontoxic to BMSCs, thereby supporting their potential for safe application in osteogenic processes (Figure S1D).

2.3. M2M-Exos Inhibit Osteoclastogenesis In Vitro. In our exploration of M2M-Exos' impact on osteoclastogenesis, RAW264.7 cells were induced to differentiate into osteoclasts using RANKL treatment and were treated with M2M, BMSC-Exos, and M2M-Exos over a 7-day period. The efficacy of these treatments was evaluated using tartrate-resistant acid phosphatase (TRAP) staining and osteoclast counting, with results presented in Figure 3A,C. These findings highlight varying degrees of inhibition on osteoclast differentiation among the groups, with the M2M-Exos group demonstrating the most pronounced inhibitory effect. During the induction of osteoclast differentiation, moderate levels of ROS serve as a second messenger in cellular signal transduction, promoting the process of osteoclastogenesis. To assess the impact on ROS, RAW264.7 cells were loaded with the ROS-sensitive dye DCFH-DA under each intervention. The results, depicted in Figure 3B,D, show that M2M, Exos, and M2M-Exos all had significant scavenging effects on ROS generation, with M2M-Exos exhibiting superior ROS scavenging capabilities compared to M2M or BMSC-Exos alone. Additionally, significant upregulation of mRNA expression for osteoclast markers such as cathepsin K (CTSK), matrix metallopeptidase 9 (MMP-9), and nuclear factor of activated T-cells, cytoplasmic 1 (NFATc1) was observed in RANKL-treated RAW264.7 cells (Figure 3E−G). However, intervention with M2M, BMSC-Exos, and M2M-Exos resulted in varying degrees of down-regulation of these markers, with the most substantial effects noted in the M2M-Exos group. Further verification through Western blot analyses confirmed the upregulation of proteins like RANKL, CTSK, NFATc1, and TRAP, aligning with the qPCR results (Figure 3H−L). These findings clearly indicate that while both M2M and BMSC-Exos significantly inhibit

https://doi.org/10.1021/acsami.4c22304
ACS Appl. Mater. Interfaces 2025, 17, 22279−22292

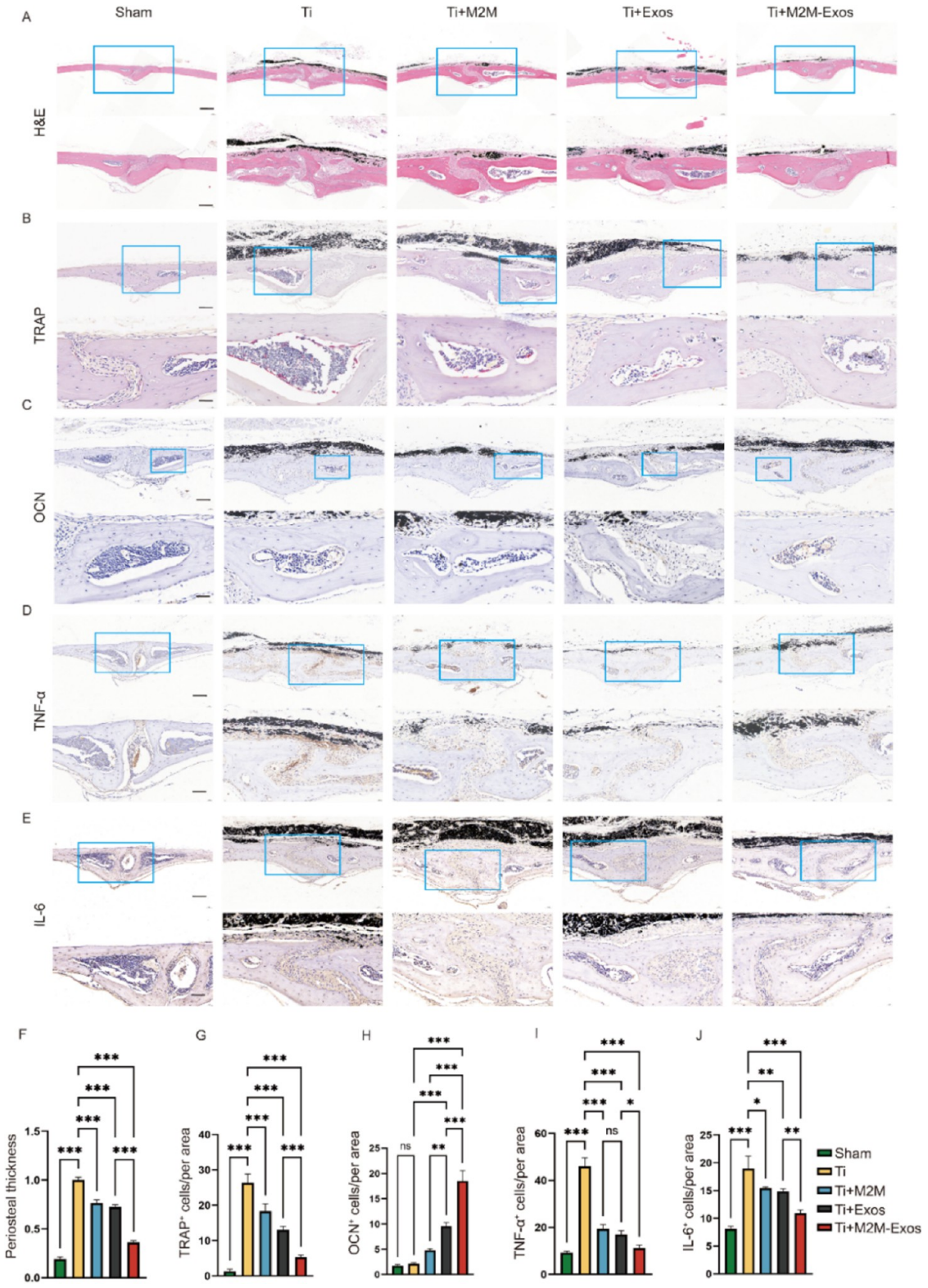

Figure 7. Histological staining and morphometric analysis of skull sections. (A, F) H&E staining with corresponding enlarged regions and quantitative analysis of periosteal thickness. (Scale bars,100 μm (top), 50 μm (bottom)) (B, G) TRAP staining with corresponding enlarged regions and quantitative analysis of TRAP-positive cells. (Scale bars,100 μm (top), 20 μm (bottom)) (C, H) Representative images of OCN staining, with quantitative analysis of OCN-positive area. (Scale bar,100 μm (top), 20 μm (bottom)). (D, I) Representative images of TNF-α staining, with quantitative analysis of TNF-α-positive area. (Scale bars,100 μm (top), 50 μm (bottom)) (E, J) Representative images of IL-6 staining, with quantitative analysis of IL-6-positive area. (Scale bars,100 μm (top), 20 μm (bottom)) (*p < 0.05, **p < 0.01, ***p < 0.001).

osteoclast differentiation, the inhibitory impact of M2M-Exos is more pronounced than either alone.

2.4. M2M-Exos Inhibit Inflammation In Vitro. In exploring the role of M2M-Exos in modulating inflammation,

https://doi.org/10.1021/acsami.4c22304
ACS Appl. Mater. Interfaces 2025, 17, 22279−22292

we induced RAW264.7 cells with lipopolysaccharide (LPS) to trigger an inflammatory response. The qPCR results indicated a significant increase in the expression of inflammatory cytokines IL-1β, IL-6, and TNF-α in LPS-induced RAW264.7 cells. However, treatment with M2M, BMSC-Exos, and M2M-Exos resulted in varying degrees of down-regulation of these inflammatory mediators (Figure 4A−C). Notably, M2M-Exos demonstrated a significant decrease in the upregulation of IL-1β, IL-6, and TNF-α mRNA expressions compared to treatments with either M2M or BMSC-Exos alone. Subsequent Western blot analyses corroborated these findings, showing that LPS upregulated the expression of IL-1β, IL-6, and TNF-α in RAW264.7 cells (Figure 4D−G). The M2M-Exos group displayed a more effective inhibition of these inflammatory factors compared to the M2M and BMSC-Exos groups. This suggests that M2M-Exos may have a potent anti-inflammatory effect by modulating the expression of key inflammatory cytokines. Additionally, to confirm that the observed effects were not due to cytotoxicity, dual staining for live/dead cells and CCK-8 assays were performed (Figure S1A,E). These tests demonstrated that M2M-Exos, at various concentrations ranging from 0, to 400 μg/mL, were nontoxic to RAW264.7 cells, reinforcing their suitability for therapeutic applications without adverse cell viability effects. (Figure S1B).

2.5. Intravenous Injection of M2M-Exos Targeting Resorption Particle-Induced Cranial Osteolysis Sites. To evaluate the targeting ability of M2M-Exos, we constructed a model of cranial osteolysis induced by Ti particles in mice as shown in the schematic diagram (Figure 6A). In this experiment, an in vivo imaging system (IVIS) was used to evaluate the distribution of M2M-Exos in mice after resorption particle-induced cranial osteolysis. DiR-labeled BMSC-Exos and M2M-Exos were intravenously injected 1 day after modeling. The targeting ability of M2M-Exos in Ti-induced cranial osteolysis is shown in Figure 5A. As depicted in Figure 5A, a weak fluorescent signal was observed in the control group (DiR). In contrast, the M2M-Exos group exhibited a stronger fluorescence in the resorbed bone area compared to the BMSC-Exos group. Additionally, the fluorescence intensity in the M2M-Exos group significantly increased. The fluorescence intensity in the bone resorption area of the M2M-Exos group was 1.45 times higher than that of the BMSC-Exos group ($p < 0.05$). As shown in Figure 5 B, ex vivo skull imaging of mice revealed that the M2M-Exos group had significantly stronger skull fluorescence compared to the DiR group and the BMSC-Exos group, indicating that M2M encapsulation can enhance the targeting ability of BMSC-Exos and increase the accumulation of BMSC-Exos in the bone resorption area. However, as shown in Figure 5E,F, due to the mononuclear phagocyte system, BMSC-Exos and M2M-Exos were mainly enriched in the liver and spleen in addition to the bone resorption area. These findings underscore the potential of M2M-Exos for targeted therapeutic applications in conditions involving bone resorption, such as osteolysis, while also pointing to challenges related to off-target accumulation and clearance.

2.6. Treatment of Ti Granule-Induced Cranial Osteolysis by Intravenous Injection of M2M-Exosomes. To evaluate the therapeutic efficacy of M2M-Exos in treating periprosthetic osteolysis, cranial osteolysis was induced using titanium (Ti) granules (Figure 6A). Weekly intravenous injections of DiR, M2M, BMSC-Exos, or M2M-Exos (200 μg) were administered via the tail vein of mice. The extent of cranial osteolysis was assessed through microcomputed tomography (micro-CT) scanning and three-dimensional reconstruction. Compared to the sham operation group, the Ti granule-induced group exhibited more pronounced osteolysis. The three intervention groups demonstrated varying degrees of osteolysis inhibition, with the M2M-Exos group showing a superior inhibitory effect compared to the M2M and BMSC-Exos groups (Figure 6B). Parameters such as bone volume/total volume (BV/TV), bone surface area/bone volume (BS/BV), and porosity related to osteolysis were measured. M2M-Exos treatment significantly increased BV/TV compared to the BMSC-Exos and M2M groups (Figure 6D). Following Ti treatment, cranial erosion was markedly enhanced; however, M2M-Exos significantly improved skull BS/BV and porosity compared to the M2M and BMSC-Exos groups (Figure 6C,E).

Hematoxylin and eosin (H&E) staining of cranial sections from experimental mice revealed fewer inflammatory responses and bone lysis changes in the sham operation group. In contrast, Ti powder coating led to evident inflammatory reactions and bone lysis, with periosteal thickening observed. The M2M, BMSC-Exos, and M2M-Exos groups displayed reduced inflammation, osteolytic changes, and periosteal thickness compared to the Ti group (Figure 7A).

TRAP staining indicated a higher number of TRAP-positive cells on the skull surface in the Ti group compared to the sham operation group. The number of TRAP-positive cells was significantly reduced in the three intervention groups relative to the Ti group, with the M2M-Exos group showing the lowest number of TRAP-positive cells among the groups (Figure 7B). Osteogenic marker osteocalcin (OCN) was highly expressed in the M2M-Exos treatment group (Figure 7C). Additionally, the expressions of IL-6 and TNF-α were elevated in the Ti group, predominantly around the osteolysis region. In contrast, the M2M-Exos group exhibited lower levels of IL-6 and TNF-α compared to the M2M and BMSC-Exos groups (Figure 7D,E). In addition, ELISA results showed that M2M-Exos significantly reduced the release of serum inflammatory factors in the model mice (Figure S1I). These findings suggest that M2M-Exos is more effective in mitigating sterile inflammation induced by Ti, promoting osteogenesis, and reducing osteoclast formation compared to M2M and BMSC-Exos alone.

3. DISCUSSION

In this study, we induced inflammatory bone resorption within the skull matrix using Ti powder metal particles. Titanium metal, known for its exceptional biocompatibility, does not cause rejection or allergic reactions and possesses robust corrosion resistance. Its high strength and low density allow artificial implants made from titanium to provide substantial mechanical support. Previous studies have shown that prolonged friction may generate small particles from these implants. These wear debris trigger peri-implant bone resorption, leading to aseptic loosening. This process involves particles at the bone-implant interface activating macrophages, fibroblasts, and multinucleated giant cells in the connective tissue,[38] which release cytokines such as ROS TNF-α, IL-1β, IL-6, IL-17, IFN-γ, and M-CSF.[39] This inflammatory condition perpetuates the acquired immune response, with macrophages recruited producing ROS and nitric oxide (NO), fostering osteoclast differentiation, and triggering apoptosis in CD4+ T lymphocytes. These lymphocytes are drawn to areas with wear debris or chronic inflammation, and osteoclast activation is

https://doi.org/10.1021/acsami.4c22304
ACS Appl. Mater. Interfaces 2025, 17, 22279−22292

further enhanced by RANKL, while OPG, an inhibitor of the RANK−RANKL signaling pathway, is suppressed, leading to further bone loss. The internalization of wear debris also impairs osteoblast functions, exacerbating bone resorption.[40,41] Our experimental findings reveal that M2M-Exos effectively harness specific surface markers on M2M. In vivo imaging experiments in mice showed that M2M-Exos, compared to pure DiR-labeled exosomes, demonstrated marked targeting specificity to the inflamed areas of skull bone resorption, suggesting an inheritance of the intrinsic biological functions of the external cell membrane. Consequently, we propose that M2M-Exos can precisely identify and target specific cell types, simulating natural cell−cell communication mechanisms. This enables a more accurate delivery of their encapsulated BMSC-Exos. Moreover, compared to conventional drug delivery systems, M2M-Exos display lower immunogenicity and improved biocompatibility, providing a biological basis for extending the half-life of engineered exosomes in biological systems.

Cell membrane-encapsulated nanoparticles have demonstrated significant potential in numerous studies.[42−44] The modification and functionalization of exosomes focus on two main strategies: chemical and genetic modification.[45] Chemical modification typically involves altering specific ligands or antibodies on the exosome surface to enhance recognition, binding, and therapeutic delivery to target cells or tissues. In contrast, genetic modification uses genetic engineering techniques to create cells that secrete exosomes equipped with tailored targeting and functional molecules. However, due to the complexity of synthesis and the inconsistent quality of chemically modified exosomes, there has been a shift toward biomimetic nanocarriers. These are often cloaked with a single macrophage membrane or combinations of macrophage membranes, such as those incorporating elements from bacterial and synthetic lipid membranes.[46−48] Upon accumulating in inflamed tissues, these nanoparticles loaded with exosomes react to locally elevated levels of ROS and release their contents to provide effective biological treatments. Furthermore, the presence of specific membrane antigens like TNFR2, CD36, and CCR2 enables these nanoparticles,[49] particularly those cloaked with M2 macrophage membranes, to bind effectively and blend in with various pro-inflammatory cytokines and chemokines. Research has shown that M2 macrophage membrane-encapsulated exosomes can engage with receptors on target cells through their surface proteins, facilitating precise recognition and targeted delivery to specific cell types. This unique targeting capability is likely attributed to the specific proteins and RNA present on their surfaces.[42,50,51] The chemokine receptor CCR2, highly expressed on M2M, enables recognition of inflammation-derived chemokines (e.g., CCL2)[52,53] directing M2M-coated nanoparticles toward inflammatory microenvironments.[51] Additionally, integrins ($\alpha D\beta 2$, $\alpha M\beta 2$) and scavenger receptors (CD163, CD206) enriched on M2M enhance cellular motility while enabling specific recognition of pathological markers (e.g., tumor-associated antigens or inflammation-specific proteins), thereby augmenting targeting precision.[54] This multireceptor-mediated targeting mechanism confers superior specificity and efficiency to M2M-coated nanoparticles in both inflammatory and oncological contexts.

This study has substantiated through both cellular and animal experiments that M2M-Exos can effectively curb the upregulation of inflammatory cytokines such as IL-1β, IL-6, and TNF-α in areas of inflammatory bone resorption surrounding implants. This observation warrants further investigation. Upon reaching the targeted areas, M2M-Exos gradually release BMSC-Exos, which serve to mitigate inflammation in the bone resorption zones. BMSC-Exos are known to harbor a variety of anti-inflammatory and growth factors, including transforming growth factor-β (TGF-β), interleukin-10 (IL-10), and tumor necrosis factor-stimulated gene (TSG-6).[55] They also contain miRNAs that participate in immune-related pathways, such as miR-301a, miR-22, and miR-let-7.[56] The multifunctional transcription factor NF-κB, which is pivotal in inflammation and osteoclastogenesis,[57] is also downregulated by BMSC-Exos in inflammatory models.[50] Additionally, the transforming growth factor (TGF) and insulin-like growth factor (IGF)[58] present on the surface of M2 macrophage membranes contribute anti-inflammatory effects by suppressing the activation of immune cells and the release of inflammatory mediators, thereby diminishing the inflammatory response.

While M2M-Exos hold considerable promise, there are critical areas in their design and production that require enhancements. The process of exosome production, for example, needs optimization to boost both yield and stability. Additionally, issues such as the source of exosomes, their purification methods, and stringent quality control measures necessitate further development. Techniques like flow cytometry could be employed in the selection and purification of BMSCs primary cells to ensure cellular homogeneity and minimize potential interference. Moreover, the choice of cell membrane for encapsulation, currently derived from M2 macrophages induced in RAW264.7 cells using IL-4 and IL-13, presents another challenge. Macrophages can differentiate into various subtypes based on the stimulating factors,[59] altering the types and ratios of receptors and ligands on the cell membrane surface. Exploring alternative cell membrane sources that target inflammation more effectively could enhance the therapeutic potential of exosomes. Our investigations have sparked new design concepts for the clinical application of exosomes, suggesting innovative approaches for managing peri-implant bone resorption and advancing treatment modalities.

4. CONCLUSIONS

In our study, we successfully extracted BMSC-Exos and M2M, and constructed M2M-Exos using a lipid coextrusion device. We evaluated the inhibitory effects on bone resorption, anti-inflammatory properties, and bone regeneration promotion of M2M-Exos in vitro. The targeting and therapeutic effects were assessed in a mouse calvarial osteolysis model. We hypothesized that M2M-Exos could target the area of bone resorption, releasing exosomes and cell membranes together to exert anti-inflammatory effects. Our delivery system provides an effective biological strategy for preventing.

5. EXPERIMENTAL SECTION

5.1. Extracellular Vesicle Isolation. We isolated cultured BMSCs using the method described previously.[60] The BMSC culture medium consists of 89% DMEM (Gibco, New York), 10% fetal bovine serum (FBS,Umibio(Shanghai)Co.,Ltd.), and 1% penicillin-streptomycin solution (Procell, Wuhan, China). When BMSCs reach 70% confluence, they are washed 3 times with phosphate-buffered saline (PBS) (ABclonal Technology, WuHan, China). The cell culture supernatant is then collected after culturing in exosome-free medium

https://doi.org/10.1021/acsami.4c22304
ACS Appl. Mater. Interfaces 2025, 17, 22279−22292

for 2 days. The collected supernatant is centrifuged at 4 °C, and the resulting cell-free supernatant undergoes further centrifugation at 300*g* for 10 min, 2000*g* for 30 min, and 4000*g* for 30 min. The postcentrifugation supernatant is filtered through a 0.2 μm filter, added to an Amicon Ultra-15 centrifugal filter unit (10 kDa), and centrifuged at 4000*g* for 15 min. Exoquick TC (System Biosciences, Bay Area, California) is added to the ultrafiltration solution, mixed thoroughly, and left to stand for 12 h. The mixture is then centrifuged at 1500*g* for 30 min to obtain exosomes. The protein content of the exosomes is determined using the Bicinchoninic Acid Assay (BCA) protein analysis kit (New Cell & Molecular Biotech Co. Ltd., Suzhou, China).

5.2. M2 Macrophage Membrane Extraction. RAW264.7 cells were obtained from Procell (Wuhan, China), and the culture medium consists of 89% high-glucose DMEM (CYTOCH, Shanghai, China), 10% FBS (YALI (Jiangsu) Biotech Co., Ltd.), and 1% penicillin-streptomycin solution (Gibco, New York). After expanding RAW264.7 cells, they were induced to differentiate into M2 macrophages using complete medium containing 20 ng/mL IL-4 and 10 ng/mL IL-13 cytokines. M2 macrophages were scraped, and the cell pellet was obtained by centrifugation. The cells were washed 3 times with PBS, and cell membranes were extracted by adding 10 mL of double-distilled water, disrupting the cell membrane by repeated sonication at 100 W for 5 min (5 s on, 5 s off). The M2 macrophage membrane was extruded at least 20 times through a 200 nm filter using a lipid extruder (Avestin, Germany). After centrifugation at 14,000*g* for 30 min, the cell membrane was collected and purified by washing twice with cold Tris-magnesium buffer (TM buffer, pH 7.4, 0.01 M Tris, 0.001 M MgCl2) in the presence of 0.25 M sucrose. The protein content of the M2M was determined using BCA, and M2M was stored at −80 °C.

5.3. M2M-Exos Preparation. The protein content of M2M and Exos was determined using the BCA protein analysis method. M2M and Exos were mixed in various protein content ratios (1:2, 2:3, 1:1, 3:2, 2:1) in PBS containing 5% poly(ethylene glycol). The M2M-Exos were extruded at least 20 times through a 200 nm filter using a lipid extruder (Avestin, Germany). Particle size was analyzed using a nanoparticle tracking analyzer (NanoSight NS300), and the ultrastructure was observed via transmission electron microscopy. M2M and Exos were labeled with DiI (Beyotime, Shanghai, China) and DiO (Beyotime, Shanghai, China), respectively. The encapsulation efficiency of different M2M-Exos ratios was analyzed using the VSSC mode of a Cytoflex flow cytometer. Cellular uptake of M2M-Exos was observed using laser confocal microscopy (with DiO-labeled M2M and DiI-labeled Exos).

5.4. Coomassie Brilliant Blue Staining. After electrophoresis, a portion of the gel containing the marker protein and a small amount of the sample was stained by placing the gel in Coomassie Brilliant Blue staining solution (Share-bio, ShangHai). The gel was gently shaken on a horizontal shaker at room temperature for 1 h. After removing the staining solution, an appropriate amount of Coomassie Brilliant Blue destaining solution was added to fully cover the gel. The gel was gently shaken on a horizontal shaker at room temperature for 12 h. The destaining solution was changed 2−4 times during this period until the blue background was mostly removed.

5.5. qPCR Analysis. Total RNA was extracted from experimental samples using SteadyPure Universal RNA extraction Kit (ACCURATE BIOTECHNOLOGY (HUNAN) CO., LTD, Changsha, China) and quantified by spectrophotometry. Complementary DNA (cDNA) synthesis was performed with 1 μg RNA through reverse transcription. qPCR reactions (20 μL) containing SYBR Green Master Mix (10 μL) (APExBIO, Houston), gene-specific primers (0.4 μM each), cDNA template (2 μL), and nuclease-free water were prepared in triplicate, including no-template controls and reference gene reactions. Thermal cycling parameters comprised initial denaturation (95 °C, 3 min), 40 cycles of amplification (95 °C/15 s; primer-specific annealing temperature/30 s with fluorescence acquisition), followed by melt curve analysis (95 → 60 → 95 °C, 0.3 °C/s increment) to confirm amplicon specificity. Relative quantification was determined using the 2∧(−ΔΔCt) method with β-actin as endogenous control. All procedures were conducted under RNase-free conditions

5.6. Western Blot Analysis. Cells were washed with PBS, and proteins were lysed using RIPA buffer (Shanghai Life-iLab Biotech Co. Ltd) containing protease and phosphatase inhibitors. Protein concentration was quantified using the BCA, and the proteins were boiled in Laemmli buffer for 5 min. Thirty micrograms of protein were separated by sodium dodecyl sulfate−polyacrylamide gel electrophoresis (SDS−PAGE) and transferred to a poly(vinylidene difluoride) (PVDF) membrane (Millipore, MA). The membrane was blocked with 5% BSA (Sigma) at room temperature for 1 h. Primary antibodies, diluted according to the manufacturer's instructions, were incubated with the membrane overnight at 4 °C. The primary antibodies used were: anti-Integrin β1 (Abcam, U.K.), anti-CD63 (Abcam, U.K.), and anti-TSG101 (Abcam, U.K.). Subsequently, species-specific horseradish peroxidase (HRP)-conjugated secondary antibodies (VivaCell, Shanghai, China) were applied. The immunereactive proteins were detected using a chemiluminescence kit (FD8030, Fudebio, China), and the signal was captured using a ChemiDoc XRS (Bio-Rad).

5.7. CCK-8 Cytotoxicity Assay. RAW264.7 and BMSC cell suspensions were seeded in a 96-well plate (100 μL per well) (NEST Biotechnology), with 5000 cells per well. After 24 h ours, intervention stimuli were applied, and the cells were cultured. After another 24 h, 10 μL of CCK-8 solution was added to each well, including a blank control well. The plate was then placed in a cell culture incubator for an additional 2 h. Finally, absorbance was measured using an ELISA reader at 450 nm.

5.8. Flow Cytometry. RAW264.7 cells were seeded in a 6-well plate (1×10^5 cells per well) and cultured in M2-inducing medium, composed of 89% high-glucose DMEM, 10% FBS (JYK-FBS-301, INNER MONGOLIA JIN YUAN KANG BIOTECHNOLOGY CO., LTD.), and 1% penicillin-streptomycin solution (Gibco, New York), supplemented with 20 ng/mL IL-4 and 10 ng/mL IL-13 (PeproTech Inc., Westlake Village). The cells were incubated overnight. After intervention, the RAW264.7 cell suspension was collected, centrifuged, and the culture medium was removed to obtain the cell pellet. The pellet was washed with PBS to remove residual medium and contaminants. The cells were sequentially labeled with CD206 and F4/80. After resuspension in PBS, the suspension was analyzed using a Cytoflex flow cytometer to detect fluorescently labeled antibodies and other parameters in SSC mode.

5.9. Osteogenic Differentiation. 1×10^5 BMSC cells were seeded in a 48-well plate and cultured in osteogenic induction medium (OriCell, from Cyagen Biosciences (Guangzhou)Inc.). After osteogenic stimulation, assays for ALP activity, ALP staining, ARS staining, and Von Kossa staining (Solarbio, Beijing, China) were performed.

5.10. Osteoclast Differentiation. Forty-8 h after seeding 10,000 RAW264.7 cells in a 48-well plate, cells were cultured in complete osteoclast medium containing 1 mg/mL Ti, 100 ng/mL RANKL (R&D Systems, Minnesota), and 300 μg/mL of M2M, BMSC-Exos, or M2M-Exos. After 7 days, the osteoclasts were stained using a TRAP assay kit (Sigma-Aldrich). TRAP-positive osteoclasts (>3 nuclei) in each well were counted under an inverted microscope.

5.11. ROS Assay. RAW264.7 cell suspensions were seeded in a 48-well plate (500 μL per well), with 2 × 10 ∧ 4 cells per well. DCFH-DA was diluted in serum-free culture medium at a ratio of 1:1000 to achieve a final concentration of 10 μmol/L. After 24 h, the cell culture media were removed, and 500 μL of the diluted DCFH-DA solution was added to each well. The plate was incubated for 20 min in a cell culture incubator. Cells were washed 3 times with serum-free medium to remove unincorporated DCFH-DA. Using an excitation wavelength of 488 nm and an emission wavelength of 525 nm, the plate was observed and photographed under an inverted fluorescence microscope.

5.12. Mouse Calvarial Osteolysis Model Construction. Animal experiments were approved by the Zhejiang University Animal Experiment Management Committee and conducted in accordance with the principles outlined in the Guidelines for the

https://doi.org/10.1021/acsami.4c22304
ACS Appl. Mater. Interfaces 2025, 17, 22279−22292

Care and Use of Laboratory Animals. A skull bone resorption model was established in 8-week-old male C57BL/6J mice using Ti particles. Mice were randomly divided into five groups: sham surgery group, Ti group, Ti + M2M group, Ti + BMSC-Exos group, and Ti + M2M-Exos group. Surgical instruments were sterilized, and mice were anesthetized prior to a sagittal incision extending from the midpoint between the eyes to the midpoint between the ears. The skull surface was exposed, the periosteum was scraped off, and 30 mg of Ti particles were evenly distributed over the skull. The sham surgery group underwent only periosteum removal. On days 1, 8, 15, and 22 postmodeling, DiR, Exos, and M2M-Exos were administered via tail vein injections. Mice were euthanized on day 28, skull slices were collected, and major organs were fixed.

Micro-CT imaging (Skyscanner 1176; Skyscanner, Aartselaar, Belgium) was employed for histological analysis of the mouse skulls. Scanning parameters were set to 400 μA per pixel, 50 kV, and 8.88 μm resolution. Following reconstruction, parameters including bone surface area to bone volume ratio (BS/BV), bone volume to total volume ratio (BV/TV), and porosity were assessed in the region of interest (ROI). Skull slices were decalcified in 10% EDTA for 1 week, stained with hematoxylin and eosin (HE) and tartrate-resistant acid phosphatase (TRAP), and subsequently scanned using a 3DHISTECH P250 FLASH scanner.

5.13. In Vivo Imaging. An induced skull bone resorption model using Ti particles (Nanjing Emperor Nano Materials, China) was established in 8-week-old male C57bL/6j mice. One day postmodeling, DiR and DiR-labeled BMSC-Exos and M2M-Exos (100 μL, 200 μg) were injected into the tail vein. Fluorescent images were captured at 24, 48, and 72 h using an IVIS (Caliper). Mice were euthanized at 72 h, skulls and organs were isolated, and the distribution of DiR, Exos, and M2M-Exos in the skulls and organs was analyzed. IVIS was used to analyze the fluorescence intensity of the backgrounds of skulls and organs in each group.

5.14. Immunohistochemistry. Skull slices were rehydrated, microwaved, and examined for histological changes in OCN, IL-6, and TNF-α. Slices were then incubated overnight at 4 °C with primary antibodies against OCN (Abcam, U.K.), RANKL (Abcam, U.K.), IL-6 (Abcam, U.K.), and TNF-α (Abcam, U.K.), followed by secondary antibodies (1:2000; Abcam, U.K.) for 1 h at room temperature. Images were captured using an optical microscope (Nikon, Japan). Positive areas and cell counts were evaluated in nonbone tissue adjacent to the midline suture in five randomly selected fields (250 μm × 500 μm) using ImageJ software for ROI analysis.

5.15. H&E Staining. To prepare for staining, slides were heated in a 65 °C oven for 10 min to melt the paraffin. Sections were deparaffinized in xylene for 3−5 min, repeated twice. The sections underwent a graded dehydration process in ethanol at concentrations of 100, 95, 70, and 50%, each for 5 min. Hematoxylin staining was performed for 3 min, followed by rinsing in tap water and brief dipping in acid alcohol (e.g., hydrochloric acid alcohol) for 5 s. After another rinse, the sections were stained with eosin for 1 min. They were then dehydrated in ethanol, cleared in xylene, and finally coverslipped.

5.16. Confocal Cell Uptake. Cells were plated at a density of 1×10^5 cells per well in confocal cell culture dishes and incubated overnight to adhere. Subsequently, DiO- labeled M2M or DiI-labeled BMSC-Exos, or M2M-Exos were added to the wells based on the experimental groups. The cells were incubated for 3 h to allow for uptake, which was then assessed using a Zeiss inverted laser confocal microscope. Appropriate laser excitation wavelengths and fluorescence filters were employed to visualize the uptake phenomena.

5.17. Immunofluorescence Staining. RAW264.7 cells grown on poly-L-lysine-coated glass coverslips in 24-well plates were fixed with 4% paraformaldehyde for 15 min at room temperature (RT), followed by three 5 min PBS washes. For intracellular antigen detection, cells were permeabilized with 0.1% Triton X-100/PBS for 10 min and rinsed thrice with PBS. Nonspecific binding was blocked with 5% Goat Serum for Blocking (Biodragon, AbBox, China) for 1 h at RT. Primary antibodies diluted in blocking buffer (Biodragon, AbBox, China) were applied overnight at 4 °C. After three 5 min PBS washes, species-matched fluorescent secondary antibodies (1:1000) were incubated for 1 h at 37 °C protected from light. Cell nuclei were counterstained with DAPI (1 μg/mL) for 5 min, followed by two 3 min PBS rinses. Coverslips were mounted using antifade mounting medium and sealed with nail polish. Images were acquired using a fluorescence microscope with sequential channel capture to prevent crosstalk.

5.18. Data Analysis. Data are presented as mean ± standard deviation (SD). The study was conducted 3 times to ensure reliability. For multiple comparisons, one-way analysis of variance (ANOVA) was applied. Data analysis was performed using GraphPad Prism 9 and ImageJ software. Statistical significance was established at a p-value <0.05; "N.S." denotes not significant. Significance levels were denoted as $*p < 0.05$, $**p < 0.01$, $***p < 0.001$.

■ ASSOCIATED CONTENT

Data Availability Statement

The data that support the findings of this study are available from the corresponding author upon reasonable request.

Supporting Information

The Supporting Information is available free of charge at https://pubs.acs.org/doi/10.1021/acsami.4c22304.

M2M-Exos cytotoxicity test + phagocytosis of M2-Exos by BMSC cells (PDF)

■ AUTHOR INFORMATION

Corresponding Authors

Yihe Hu − *Department of Orthopedics, The First Affiliated Hospital, Zhejiang University School of Medicine, Hangzhou, Zhejiang 310003, China*; Email: xy_huyh@163.com

Jie Xie − *Department of Orthopedics, The First Affiliated Hospital, Zhejiang University School of Medicine, Hangzhou, Zhejiang 310003, China*; orcid.org/0000-0001-8042-0600; Email: dr_xiejie@zju.edu.cn

Authors

Zheyu Zhang − *Department of Orthopedics, The First Affiliated Hospital, Zhejiang University School of Medicine, Hangzhou, Zhejiang 310003, China*

Tianliang Ma − *Department of Orthopedics, The First Affiliated Hospital, Zhejiang University School of Medicine, Hangzhou, Zhejiang 310003, China*

Qimeng Liu − *Department of Orthopedics, The First Affiliated Hospital, Zhejiang University School of Medicine, Hangzhou, Zhejiang 310003, China*

Jiangyu Nan − *Department of Orthopedics, The First Affiliated Hospital, Zhejiang University School of Medicine, Hangzhou, Zhejiang 310003, China*

Guanzhi Liu − *Department of Orthopedics, The First Affiliated Hospital, Zhejiang University School of Medicine, Hangzhou, Zhejiang 310003, China*

Yute Yang − *Department of Orthopedics, The First Affiliated Hospital, Zhejiang University School of Medicine, Hangzhou, Zhejiang 310003, China*

Complete contact information is available at: https://pubs.acs.org/10.1021/acsami.4c22304

Author Contributions

†Z.Z. and T.M. contributed equally to this work. Z.Z.: conceptualization, investigation, methodology, writing—original draft. T.M.: methodology, writing—review & editing. Q.L.: formal analysis, writing—review & editing. J.N.: software, data curation. G.L., Y.Y.: methodology, investigation, software. J.X.:

https://doi.org/10.1021/acsami.4c22304
ACS Appl. Mater. Interfaces 2025, 17, 22279−22292

supervision, writing—review & editing, funding support. Y.H.: supervision, funding support.

Funding

This work was supported by the National Natural Science Foundation of China under grant numbers 82372414,82272452 and 82202733 and the Zhejiang Provincial Natural Science Foundation of China under grant number LQN25H060009.

Notes

The authors declare no competing financial interest.

■ ACKNOWLEDGMENTS

We would like to express our sincere gratitude to Biorender for their invaluable support in the creation of the Graphical Abstract presented in this manuscript. Thanks for the technical support by the core Facilities, the First Affiliated Hospital Zhejiang University School of Medicine.

■ REFERENCES

(1) Desai, M. A.; Bancroft, L. W. The case. Diagnosis: periprosthetic osteolysis. *Orthopedics* **2008**, *31* (6), 518−615-8 518.
(2) Dubin, J. A.; Bains, S. S.; Paulson, A. E.; Monarrez, R.; Hameed, D.; Nace, J.; Mont, M.; Delanois, R. E. The Current Epidemiology of Revision Total Knee Arthroplasty in the United States From 2016 to 2022. *J. Arthroplasty* **2024**, *39* (3), 760−765.
(3) Delanois, R. E.; Mistry, J. B.; Gwam, C. U.; Mohamed, N. S.; Choksi, U. S.; Mont, M. A. Current Epidemiology of Revision Total Knee Arthroplasty in the United States. *J. Arthroplasty* **2017**, *32* (9), 2663−2668.
(4) Lee, G. W.; Lee, K. B. Periprosthetic Osteolysis as a Risk Factor for Revision After Total Ankle Arthroplasty: A Single-Center Experience of 250 Consecutive Cases. *J. Bone Jt. Surg.* **2022**, *104* (15), 1334−1340.
(5) Morcos, M. W.; Kooner, P.; Marsh, J.; Howard, J.; Lanting, B.; Vasarhelyi, E. The economic impact of periprosthetic infection in total knee arthroplasty. *Can. J. Surg.* **2021**, *64* (2), E144−E148.
(6) Bertrand, J.; Delfosse, D.; Mai, V.; Awiszus, F.; Harnisch, K.; Lohmann, C. H. Ceramic prosthesis surfaces induce an inflammatory cell response and fibrotic tissue changes. *Bone Jt. J.* **2018**, *100-B* (7), 882−890.
(7) Gallo, J.; Goodman, S. B.; Konttinen, Y. T.; Wimmer, M. A.; Holinka, M. Osteolysis around total knee arthroplasty: a review of pathogenetic mechanisms. *Acta Biomater.* **2013**, *9* (9), 8046−8058.
(8) Gallo, J.; Goodman, S. B.; Konttinen, Y. T.; Raska, M. Particle disease: biologic mechanisms of periprosthetic osteolysis in total hip arthroplasty. *Innate Immun.* **2013**, *19* (2), 213−224.
(9) Anderson, J. M.; Rodriguez, A.; Chang, D. T. Foreign body reaction to biomaterials. *Semin. Immunol.* **2008**, *20* (2), 86−100.
(10) Konttinen, Y. T.; Pajarinen, J.; Takakubo, Y.; Gallo, J.; Nich, C.; Takagi, M.; Goodman, S. B. Macrophage polarization and activation in response to implant debris: influence by "particle disease" and "ion disease". *J. Long-Term Eff. Med. Implants* **2014**, *24* (4), 267−281.
(11) Goodman, S. B.; Gibon, E.; Gallo, J.; Takagi, M. Macrophage Polarization and the Osteoimmunology of Periprosthetic Osteolysis. *Curr. Osteoporos Rep.* **2022**, *20* (1), 43−52.
(12) Rao, A. J.; Gibon, E.; Ma, T.; Yao, Z.; Smith, R. L.; Goodman, S. B. Revision joint replacement, wear particles, and macrophage polarization. *Acta Biomater.* **2012**, *8* (7), 2815−2823.
(13) Perino, G.; Sunitsch, S.; Huber, M.; Ramirez, D.; Gallo, J.; Vaculova, J.; Natu, S.; Kretzer, J. P.; Muller, S.; Thomas, P.; Thomsen, M.; Krukemeyer, M. G.; Resch, H.; Hugle, T.; Waldstein, W.; Boettner, F.; Gehrke, T.; Sesselmann, S.; Ruther, W.; Xia, Z.; Purdue, E.; Krenn, V. Diagnostic guidelines for the histological particle algorithm in the periprosthetic neo-synovial tissue. *BMC Clin. Pathol.* **2018**, *18*, No. 7.
(14) Ingham, E.; Green, T. R.; Stone, M. H.; Kowalski, R.; Watkins, N.; Fisher, J. Production of TNF-alpha and bone resorbing activity by macrophages in response to different types of bone cement particles. *Biomaterials* **2000**, *21* (10), 1005−1013.
(15) Tan, S.; Wu, T.; Zhang, D.; Zhang, Z. Cell or cell membrane-based drug delivery systems. *Theranostics* **2015**, *5* (8), 863−881.
(16) Wu, Z.; Zhang, H.; Yan, J.; Wei, Y.; Su, J. Engineered biomembrane-derived nanoparticles for nanoscale theranostics. *Theranostics* **2023**, *13* (1), 20−39.
(17) Zhang, W.; Huang, X. Stem cell membrane-camouflaged targeted delivery system in tumor. *Mater. Today Bio* **2022**, *16*, No. 100377.
(18) Pegtel, D. M.; Gould, S. J. Exosomes. *Annu. Rev. Biochem.* **2019**, *88*, 487−514.
(19) Zhang, L.; Deng, S.; Zhang, Y.; Peng, Q.; Li, H.; Wang, P.; Fu, X.; Lei, X.; Qin, A.; Yu, X. Homotypic Targeting Delivery of siRNA with Artificial Cancer Cells. *Adv. Healthcare Mater.* **2020**, *9* (9), No. e1900772.
(20) Gao, X.; Li, S.; Ding, F.; Liu, X.; Wu, Y.; Li, J.; Feng, J.; Zhu, X.; Zhang, C. A Virus-Mimicking Nucleic Acid Nanogel Reprograms Microglia and Macrophages for Glioblastoma Therapy. *Adv. Mater.* **2021**, *33* (9), No. e2006116.
(21) Mu, X.; Zhang, M.; Wei, A.; Yin, F.; Wang, Y.; Hu, K.; Jiang, J. Doxorubicin and PD-L1 siRNA co-delivery with stem cell membrane-coated polydopamine nanoparticles for the targeted chemoimmunotherapy of PCa bone metastases. *Nanoscale* **2021**, *13* (19), 8998−9008.
(22) Jiang, Y.; Yu, M.; Song, Z. F.; Wei, Z. Y.; Huang, J.; Qian, H. Y. Targeted Delivery of Mesenchymal Stem Cell-Derived Bioinspired Exosome-Mimetic Nanovesicles with Platelet Membrane Fusion for Atherosclerotic Treatment. *Int. J. Nanomed.* **2024**, *19*, 2553−2571.
(23) Hofer, H. R.; Tuan, R. S. Secreted trophic factors of mesenchymal stem cells support neurovascular and musculoskeletal therapies. *Stem Cell Res. Ther.* **2016**, *7* (1), No. 131.
(24) Caldwell, K. L.; Wang, J. Cell-based articular cartilage repair: the link between development and regeneration. *Osteoarthritis Cartilage* **2015**, *23* (3), 351−362.
(25) Hall, J.; Prabhakar, S.; Balaj, L.; Lai, C. P.; Cerione, R. A.; Breakefield, X. O. Delivery of Therapeutic Proteins via Extracellular Vesicles: Review and Potential Treatments for Parkinson's Disease, Glioma, and Schwannoma. *Cell Mol. Neurobiol.* **2016**, *36* (3), 417−427.
(26) Jin, Y.; Xu, M.; Zhu, H.; Dong, C.; Ji, J.; Liu, Y.; Deng, A.; Gu, Z. Therapeutic effects of bone marrow mesenchymal stem cells-derived exosomes on osteoarthritis. *J. Cell. Mol. Med.* **2021**, *25* (19), 9281−9294.
(27) Ophelders, D. R.; Wolfs, T. G.; Jellema, R. K.; Zwanenburg, A.; Andriessen, P.; Delhaas, T.; Ludwig, A. K.; Radtke, S.; Peters, V.; Janssen, L.; Giebel, B.; Kramer, B. W. Mesenchymal Stromal Cell-Derived Extracellular Vesicles Protect the Fetal Brain After Hypoxia-Ischemia. *Stem Cells Transl. Med.* **2016**, *5* (6), 754−763.
(28) Valadi, H.; Ekstrom, K.; Bossios, A.; Sjostrand, M.; Lee, J. J.; Lotvall, J. O. Exosome-mediated transfer of mRNAs and microRNAs is a novel mechanism of genetic exchange between cells. *Nat. Cell Biol.* **2007**, *9* (6), 654−659.
(29) Liu, S.; Fan, M.; Xu, J. X.; Yang, L. J.; Qi, C. C.; Xia, Q. R.; Ge, J. F. Exosomes derived from bone-marrow mesenchymal stem cells alleviate cognitive decline in AD-like mice by improving BDNF-related neuropathology. *J. Neuroinflammation* **2022**, *19* (1), No. 35.
(30) Yu, B.; Kim, H. W.; Gong, M.; Wang, J.; Millard, R. W.; Wang, Y.; Ashraf, M.; Xu, M. Exosomes secreted from GATA-4 overexpressing mesenchymal stem cells serve as a reservoir of anti-apoptotic microRNAs for cardioprotection. *Int. J. Cardiol.* **2015**, *182*, 349−360.
(31) Arslan, F.; Lai, R. C.; Smeets, M. B.; Akeroyd, L.; Choo, A.; Aguor, E. N.; Timmers, L.; van Rijen, H. V.; Doevendans, P. A.; Pasterkamp, G.; Lim, S. K.; de Kleijn, D. P. Mesenchymal stem cell-derived exosomes increase ATP levels, decrease oxidative stress and activate PI3K/Akt pathway to enhance myocardial viability and

prevent adverse remodeling after myocardial ischemia/reperfusion injury. *Stem Cell Res.* **2013**, *10* (3), 301−312.
(32) Jin, J.; Shi, Y.; Gong, J.; Zhao, L.; Li, Y.; He, Q.; Huang, H. Exosome secreted from adipose-derived stem cells attenuates diabetic nephropathy by promoting autophagy flux and inhibiting apoptosis in podocyte. *Stem Cell Res. Ther.* **2019**, *10* (1), No. 95.
(33) Dittmer, J.; Leyh, B. Paracrine effects of stem cells in wound healing and cancer progression (Review). *Int. J. Oncol.* **2014**, *44* (6), 1789−1798.
(34) Wu, S.; Sun, S.; Fu, W.; Yang, Z.; Yao, H.; Zhang, Z. The Role and Prospects of Mesenchymal Stem Cells in Skin Repair and Regeneration. *Biomedicines* **2024**, *12* (4), No. 743, DOI: 10.3390/biomedicines12040743.
(35) Zhu, Q.; Tang, Y.; Zhou, T.; Yang, L.; Zhang, G.; Meng, Y.; Zhang, H.; Gao, J.; Wang, C.; Su, Y. X.; Ye, J. Exosomes derived from mesenchymal stromal cells promote bone regeneration by delivering miR-182−5p-inhibitor. *Pharmacol. Res.* **2023**, *192*, No. 106798.
(36) Wang, Y.; Zhang, K.; Li, T.; Maruf, A.; Qin, X.; Luo, L.; Zhong, Y.; Qiu, J.; McGinty, S.; Pontrelli, G.; Liao, X.; Wu, W.; Wang, G. Macrophage membrane functionalized biomimetic nanoparticles for targeted anti-atherosclerosis applications. *Theranostics* **2021**, *11* (1), 164−180.
(37) Wang, Y.; Hou, M.; Duan, S.; Zhao, Z.; Wu, X.; Chen, Y.; Yin, L. Macrophage-targeting gene silencing orchestrates myocardial microenvironment remodeling toward the anti-inflammatory treatment of ischemia-reperfusion (IR) injury. *Bioact. Mater.* **2022**, *17*, 320−333.
(38) Shao, H.; Shen, J.; Wang, M.; Cui, J.; Wang, Y.; Zhu, S.; Zhang, W.; Yang, H.; Xu, Y.; Geng, D. Icariin protects against titanium particle-induced osteolysis and inflammatory response in a mouse calvarial model. *Biomaterials* **2015**, *60*, 92−99.
(39) Yang, C.; Liu, W.; Shan, H.; Yu, X.; Zhang, X.; Zeng, B.; Qian, Y. Naringin inhibits titanium particles-induced up-regulation of TNF-alpha and IL-6 via the p38 MAPK pathway in fibroblasts from hip periprosthetic membrane. *Connect. Tissue Res.* **2021**, *62* (5), 485−494.
(40) Zhu, S.; Hu, X.; Tao, Y.; Ping, Z.; Wang, L.; Shi, J.; Wu, X.; Zhang, W.; Yang, H.; Nie, Z.; Xu, Y.; Wang, Z.; Geng, D. Strontium inhibits titanium particle-induced osteoclast activation and chronic inflammation via suppression of NF-kappaB pathway. *Sci. Rep.* **2016**, *6*, No. 36251.
(41) Panez-Toro, I.; Heymann, D.; Gouin, F.; Amiaud, J.; Heymann, M. F.; Cordova, L. A. Roles of inflammatory cell infiltrate in periprosthetic osteolysis. *Front. Immunol.* **2023**, *14*, No. 1310262.
(42) Chen, R.; Yang, J.; Wu, M.; Zhao, D.; Yuan, Z.; Zeng, L.; Hu, J.; Zhang, X.; Wang, T.; Xu, J.; Zhang, J. M2Macrophage Hybrid Membrane-Camouflaged Targeted Biomimetic Nanosomes to Reprogram Inflammatory Microenvironment for Enhanced Enzyme-Thermo-Immunotherapy. *Adv. Mater.* **2023**, *35* (39), No. e2304123.
(43) Li, Q.; Huang, Z.; Wang, Q.; Gao, J.; Chen, J.; Tan, H.; Li, S.; Wang, Z.; Weng, X.; Yang, H.; Pang, Z.; Song, Y.; Qian, J.; Ge, J. Targeted immunomodulation therapy for cardiac repair by platelet membrane engineering extracellular vesicles via hitching peripheral monocytes. *Biomaterials* **2022**, *284*, No. 121529.
(44) Xiong, J.; Wu, M.; Chen, J.; Liu, Y.; Chen, Y.; Fan, G.; Liu, Y.; Cheng, J.; Wang, Z.; Wang, S.; Liu, Y.; Zhang, W. Cancer-Erythrocyte Hybrid Membrane-Camouflaged Magnetic Nanoparticles with Enhanced Photothermal-Immunotherapy for Ovarian Cancer. *ACS Nano* **2021**, *15* (12), 19756−19770.
(45) Danilushkina, A. A.; Emene, C. C.; Barlev, N. A.; Gomzikova, M. O. Strategies for Engineering of Extracellular Vesicles. *Int. J. Mol. Sci.* **2023**, *24* (17), No. 13247, DOI: 10.3390/ijms241713247.
(46) Chen, H.; Deng, J.; Yao, X.; He, Y.; Li, H.; Jian, Z.; Tang, Y.; Zhang, X.; Zhang, J.; Dai, H. Bone-targeted erythrocyte-cancer hybrid membrane-camouflaged nanoparticles for enhancing photothermal and hypoxia-activated chemotherapy of bone invasion by OSCC. *J. Nanobiotechnol.* **2021**, *19* (1), No. 342.
(47) Fang, R. H.; Kroll, A. V.; Gao, W.; Zhang, L. Cell Membrane Coating Nanotechnology. *Adv. Mater.* **2018**, *30* (23), No. e1706759.
(48) Wu, T.; Liu, Y.; Cao, Y.; Liu, Z. Engineering Macrophage Exosome Disguised Biodegradable Nanoplatform for Enhanced Sonodynamic Therapy of Glioblastoma. *Adv. Mater.* **2022**, *34* (15), No. e2110364.
(49) Gao, C.; Huang, Q.; Liu, C.; Kwong, C. H. T.; Yue, L.; Wan, J. B.; Lee, S. M. Y.; Wang, R. Treatment of atherosclerosis by macrophage-biomimetic nanoparticles via targeted pharmacotherapy and sequestration of proinflammatory cytokines. *Nat. Commun.* **2020**, *11* (1), No. 2622.
(50) Xu, B.; Gan, C. X.; Chen, S. S.; Li, J. Q.; Liu, M. Z.; Guo, G. H. BMSC-derived exosomes alleviate smoke inhalation lung injury through blockade of the HMGB1/NF-kappaB pathway. *Life Sci.* **2020**, *257*, No. 118042.
(51) Zhou, K.; Yang, C.; Shi, K.; Liu, Y.; Hu, D.; He, X.; Yang, Y.; Chu, B.; Peng, J.; Zhou, Z.; Qian, Z. Activated macrophage membrane-coated nanoparticles relieve osteoarthritis-induced synovitis and joint damage. *Biomaterials* **2023**, *295*, No. 122036.
(52) Li, X.; Yao, W.; Yuan, Y.; Chen, P.; Li, B.; Li, J.; Chu, R.; Song, H.; Xie, D.; Jiang, X.; Wang, H. Targeting of tumour-infiltrating macrophages via CCL2/CCR2 signalling as a therapeutic strategy against hepatocellular carcinoma. *Gut* **2017**, *66* (1), 157−167.
(53) Raghu, H.; Lepus, C. M.; Wang, Q.; Wong, H. H.; Lingampalli, N.; Oliviero, F.; Punzi, L.; Giori, N. J.; Goodman, S. B.; Chu, C. R.; Sokolove, J. B.; Robinson, W. H. CCL2/CCR2, but not CCL5/CCR5, mediates monocyte recruitment, inflammation and cartilage destruction in osteoarthritis. *Ann. Rheum. Dis.* **2017**, *76* (5), 914−922.
(54) Cui, K.; Ardell, C. L.; Podolnikova, N. P.; Yakubenko, V. P. Distinct Migratory Properties of M1, M2, and Resident Macrophages Are Regulated by α(D)β(2) and α(M)β(2) Integrin-Mediated Adhesion. *Front. Immunol.* **2018**, *9*, No. 2650.
(55) Wang, Z.; Wu, Y.; Zhao, Z.; Liu, C.; Zhang, L. Study on Transorgan Regulation of Intervertebral Disc and Extra-Skeletal Organs Through Exosomes Derived From Bone Marrow Mesenchymal Stem Cells. *Front. Cell Dev. Biol.* **2021**, *9*, No. 741183.
(56) Ma, X.; Buscaglia, L. E. B.; Barker, J. R.; Li, Y. MicroRNAs in NF-kappaB signaling. *J. Mol. Cell Biol.* **2011**, *3* (3), 159−166.
(57) Mbalaviele, G.; Novack, D. V.; Schett, G.; Teitelbaum, S. L. Inflammatory osteolysis: a conspiracy against bone. *J. Clin. Invest.* **2017**, *127* (6), 2030−2039.
(58) Louiselle, A. E.; Niemiec, S. M.; Zgheib, C.; Liechty, K. W. Macrophage polarization and diabetic wound healing. *Transl. Res.* **2021**, *236*, 109−116.
(59) Mantovani, A.; Sozzani, S.; Locati, M.; Allavena, P.; Sica, A. Macrophage polarization: tumor-associated macrophages as a paradigm for polarized M2 mononuclear phagocytes. *Trends Immunol.* **2002**, *23* (11), 549−555.
(60) Ma, T.; Chen, S.; Wang, J.; Liang, S.; Chen, M.; Liu, Q.; Zhang, Z.; Liu, G.; Yang, Y.; Hu, Y.; Xie, J. Enhanced Osteolysis Targeted Therapy through Fusion of Exosomes Derived from M2Macrophages and Bone Marrow Mesenchymal Stem Cells: Modulating Macrophage Polarization. *Small* **2024**, *20* (7), No. e2303506.